iScience

CellPress
OPEN ACCESS

Article

Structural and vibrational properties of Sb_2S_3: Practical methodologies for accelerated research and application of this low dimensional material

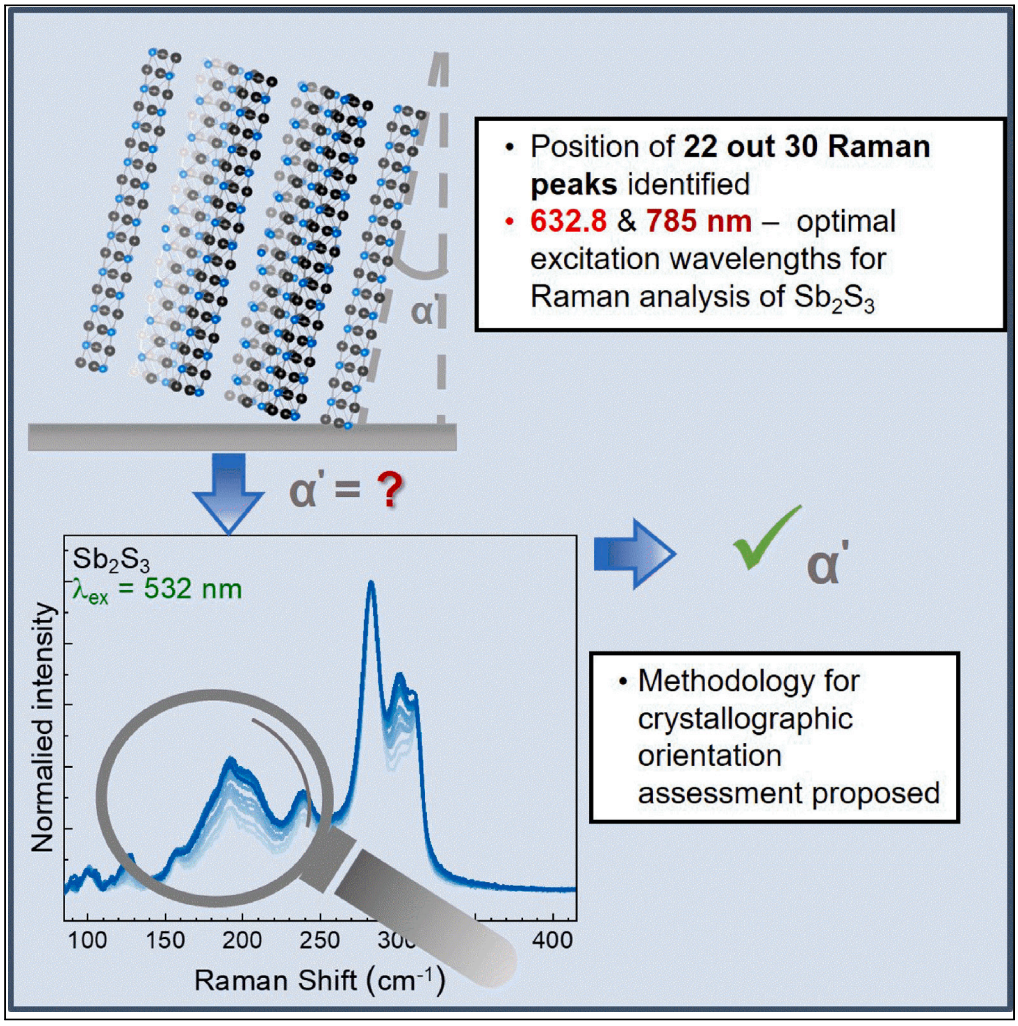

Victoria Rotaru, Pedro Vidal-Fuentes, Xavier Alcobe, ..., Ignacio Becerril-Romero, Victor Izquierdo-Roca, Maxim Guc

vizquierdo@irec.cat (V.I.-R.)
mguc@irec.cat (M.G.)

Highlights

Advanced characterization of Sb_2S_3 based on DFT, XRD, and Raman spectroscopy

Three types of Sb_2S_3 samples measured: a mineral, monograin powder, and thin films

Raman-based methodology for assessing the orientation of ribbons in Sb_2S_3 developed

Assessment of Sb_2S_3 stoichiometry by Raman, based on first principle calculations

Rotaru et al., iScience 27, 109619
April 19, 2024
https://doi.org/10.1016/j.isci.2024.109619

iScience

CellPress
OPEN ACCESS

Article

Structural and vibrational properties of Sb_2S_3: Practical methodologies for accelerated research and application of this low dimensional material

Victoria Rotaru,[1,2] Pedro Vidal-Fuentes,[1] Xavier Alcobe,[3] Tariq Jawhari,[3] Alex López-García,[1] Alejandro Pérez-Rodríguez,[1,4] Ignacio Becerril-Romero,[1] Victor Izquierdo-Roca,[1,*] and Maxim Guc[1,5,*]

SUMMARY

Recently, the interest for the family of low dimensional materials has increased significantly due to the anisotropic nature of their fundamental properties. Among them, antimony sulfide (Sb_2S_3) is considered a suitable material for various solid-state devices. Although the main advantages and physicochemical properties of Sb_2S_3 are known, some doubtful information remains in literature and methodologies to easily assess its critical properties are missing. In this study, an advanced characterization of several types of Sb_2S_3 samples, involving the Rietveld refinement of structural properties, and Raman spectroscopy analysis, completed with lattice dynamics investigations reveal important insights into the structural and vibrational characteristics of the material. Based on the gathered data, fast, non-destructive, and non-invasive methodologies for assessment of the crystallographic orientation and point defect concentration of Sb_2S_3 are proposed. With a high resolution in-sample and *in-situ* assessment, these methodologies will serve for accelerating the research and application of Sb_2S_3 in the research field.

INTRODUCTION

The low dimensional van der Waals solid antimony sulfide (Sb_2S_3) compound pertaining to the chalcogenide semiconductor family is proving to be a suitable candidate for its implementation in various research fields, such as photoelectrochemical (PEC) water reduction,[1] solar cells,[2,3] potassium-ion batteries (KIBs),[4,5] or photonic integrated circuits,[6] among others. Although the interest and number of publications related to this compound has increased considerably in the last years, it is still a challenging matter to understand the properties of Sb_2S_3 or to gather a proper picture about them on a full scale, which limits the further development of Sb_2S_3-based technologies. The main reason for this is related to the crystal structure of the compound since Sb_2S_3 crystallizes in the orthorhombic Pnma structure, forming $[Sb_4S_6]_n$ ribbons with covalently bonded atoms along the [001] crystallographic direction that are attached together by van der Waals forces along the other two directions.[7] This translates into highly anisotropic properties, which need to be considered when implementing Sb_2S_3 in electronic devices.[8,9] In order to understand the influence that the anisotropy has on the efficiency of Sb_2S_3-based devices it is essential to generate suitable assessment methodologies that provide proper insights on the fundamental properties of the compound.

In terms of fundamental properties of Sb_2S_3, reports on the structural,[1,7,10] optical,[11–13] electronic,[14–16] as well as vibrational properties[17–20] can be found. In the case of the latter, based on Raman spectroscopy (RS) measurements, there are still some doubts to be addressed about the Raman peaks and features that pertain to the Sb_2S_3 compound in order to use this technique as a practical quality control element in device fabrication. For instance, a variety of dissimilar spectra associated to Sb_2S_3 can be found in the literature,[20,21] which makes the proper assessment of samples using RS a challenging matter. Several factors contribute to these discrepancies. The main one is related to the measurement conditions employed during the studies, in particular the laser excitation wavelength and power density, which are critical for analyzing the Raman features while avoiding sample degradation that usually results in assigning of α-Sb_2O_3 characteristic peaks to the Sb_2S_3 phase.[22–25] Another important factor is related to the crystallographic orientation of the analyzed samples and its effects on the obtained Raman spectra, where the crystallographic anisotropy reflects in strong differences between the spectra observed on different crystal planes.[24]

[1]Catalonia Institute for Energy Research (IREC), Jardins de les Dones de Negre 1, 08930 Sant Adrià de Besòs, Spain
[2]Facultat de Física, Universitat de Barcelona (UB), C. Martí i Franquès 1-11, 08028 Barcelona, Spain
[3]Centres Científics i Tecnològics de la Universitat de Barcelona (CCiTUB), Lluís Solé i Sabarís 1-3, 08028 Barcelona, Spain
[4]IN^{2}UB, Departament d'Enginyeria Electrònica i Biomèdica, Universitat de Barcelona, C. Martí i Franquès 1, 08028 Barcelona, Spain
[5]Lead contact
*Correspondence: vizquierdo@irec.cat (V.I.-R.), mguc@irec.cat (M.G.)
https://doi.org/10.1016/j.isci.2024.109619

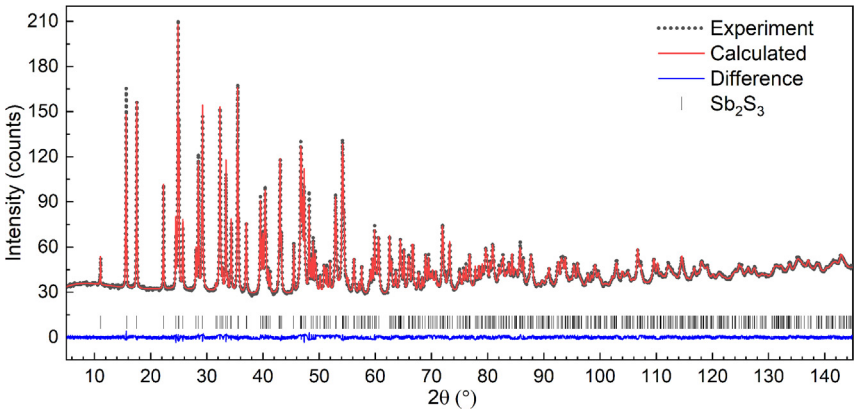

Figure 1. Rietveld refinement (red) of an XRD pattern (black) and the difference between the observed and calculated (blue) diffractograms of Sb_2S_3 powder from a single crystal

From the methodological point of view, the current assessment of the ribbons' crystallographic orientation, which is one of the most critical aspects for both materials study and application fields, is based on the assessment of the texture coefficient based on X-ray diffraction (XRD).[26] Even though it is a well-established and widely used methodology, it has several limitations related to the measurement conditions of thin film samples (usually a large measurement spot size, long measurement time, etc.) which cannot be easily overcome with typical XRD equipment. On the other hand, the recent development of RS allows this technique to go far beyond the classical assessment of vibrational properties of the materials. The improved quality of the spectra allows using RS for the assessment of several important fundamental properties of the materials. For instance, methodologies based on RS allow defining macroscopic parameters such as the thickness of nanometric layers[27,28] or the amount of atomic layers in 2D materials.[29–31] Moreover, RS is widely used to define microscopic parameters such as crystal structure, crystalline quality, chemical composition, presence of secondary phases or structural defects.[32–40]

In this work, methodologies for the assessment of Sb_2S_3 by RS are developed by a thorough experimental characterization of Sb_2S_3 by means of microprobe analysis, XRD and RS, completed with results of first-principles calculations. Different samples are employed to ensure a full understanding of the structural and vibrational properties of Sb_2S_3, specifically: a single crystal with defined facets, monograin powder obtained through milling of the single crystalline sample, and thin films. The XRD analysis is completed by a high-quality Rietveld refinement, the results of which are further employed for lattice dynamics calculations. The latter are supported by an advanced characterization of the Sb_2S_3 single crystal and powder by RS, by employing a series of different approaches: multiwavelength Raman, measurements under low temperature, and measurements under different polarization conditions. The gathered knowledge allows to propose non-invasive, high resolution in-sample and *in-situ* RS-based methodologies for the assessment of the crystallographic orientation and defect concentration in Sb_2S_3. This opens the door for accelerating the research and application of this promising low dimensional material in different fields.

RESULTS AND DISCUSSION

In order to make a thorough analysis of the fundamental properties of Sb_2S_3, three different types of samples (single crystal, powder, and thin films) were used in the present study. The powder sample was used to study the structural properties of the material by means of XRD which was completed by phase analysis and structure refinement using the Rietveld method. The chemical composition was assessed on the mineral crystal (see Figure S1) by an electron microprobe analyzer (EMPA). Finally, the vibrational properties of Sb_2S_3 were analyzed by measuring the Raman spectra of all samples using different approaches and configurations: multiwavelength approach, measurements under different polarization configurations, measurements at low temperature, and measurements using a special configuration for the analysis of the ultra-low frequency range. The experimental vibrational analysis was completed with first-principle calculations of the Raman scattering modes and of the density of phonon states. The results of these experiments are presented in the following sub-sections, together with the application of the gathered knowledge for the development of non-invasive and fast methodologies for the evaluation of the crystallographic orientation of the ribbons in Sb_2S_3 thin films and the estimation of the point defect concentration.

Structural and compositional analysis

Sb_2S_3 has a stibnite structure and crystalizes in an orthorhombic crystal lattice, space group Pnma (#62), Z = 4, with twenty atoms in the primitive unit cell, with all atoms of the asymmetric unit (two non-equivalent Sb cation sites and three non-equivalent S anions sites) in the Wyckoff Position 4c (x, $^1/_4$, z).[41,42] In the present study, high quality measurements have been performed using monograin powder obtained from a single crystalline mineral. Excellent Rietveld refinement results were obtained with R_{wp} = 4.86 and R_B = 2.10 and are presented in Figure 1.

The results of the refinement confirm the single phase of the analyzed powder, with stoichiometric composition since the best fit is obtained with site occupancy factors equal to 1 for all the atoms. The 18 refined structural parameters (three cell parameters, ten atomic coordinates, and five isotropic temperature parameters) are listed in Tables 1 and 2.

Table 1. Sb_2S_3 crystallographic parameters and refinement agreement factors

Structure, space group, Z	R_{wp}	R_B	a (Å)	b (Å)	c (Å)	V (Å^3)	V/Z (Å^3)
Orthorhombic, Pnma, 4	4.86	2.100	11.3144	3.8376	11.2326	487.715	121.929

The crystallographic results obtained in the present study are in good agreement with previous publications (e.g., see Bayliss and Nowacki,[41] and Efthimiopoulos et al.[42] and references there in) and slightly exceed them with the quality and/or precision of the performed measurements providing better results to the community to perform a more reliable modeling of the properties of the Sb_2S_3 compound and of Sb_2S_3-based devices.

The diffractogram obtained from the XRD measurement performed on the largest surface of the bulk mineral sample, shows the presence of only h00 reflections, which allows concluding that this mineral is a single crystal, and that the (100) crystallographic planes are parallel to the largest surface (see Figure S2).

WDX measurements were performed in 9 different points of the single crystalline mineral (see Figure S3). The average composition of this sample is found to be very close to stoichiometry with insignificant variations from point to point: Sb = 40.81 $\pm$ 0.22 at.% and S = 59.19 $\pm$ 0.22 at.%.

Lattice dynamics calculations

In accordance with the results of the previous section, the twenty atoms that form the unit cell of Sb_2S_3 with Stibnite structure yield a total of 60 phonon modes present in the zone-center or in the Γ-point of the Brillouin zone. From all these modes, 30 are Raman active and can be described by the following irreducible representation: $\Gamma_{Raman} = 10A_g \otimes 5B_{1g} \otimes 10B_{2g} \otimes 5B_{3g}$.[17] In accordance with this irreducible representation, no degeneration or splitting of the modes are expected, thus up to 30 first order peaks can be observed in the Raman spectrum.

To deepen in the understanding of the lattice dynamics and the fundamental vibration properties of each of the Raman peaks of Sb_2S_3, the phonon density of states (DOS), peak positions, and displacements of the vibrational modes were calculated with first-principles calculations. The phonon DOS was calculated in the Γ-point of the Brillouin zone and is depicted in Figure 2. Based on the calculation of partial DOS for each non-equivalent atom sites it is easy to conclude that in the case of low wavenumber modes (<130 cm^{-1}) mainly the vibrations of the Sb cations dominate, while in the high wavenumbers range (>130 cm^{-1}) it is the vibrations of the S anions that dominate. This gives insights into the further application of Raman spectra for the possible assessment of the structural point defects in the Sb_2S_3 compound, as will be discussed in the further sections.

Using the CASTEP tools, the Raman spectrum of Sb_2S_3 was calculated, and it is presented in Figure 2C. In this case, a temperature of 20 K has been fixed together with the smearing of the full width at half maximum (FWHM) of the peaks up to 8 cm^{-1} and using a 632.8 nm excitation wavelength. Despite some differences between the relative intensity of several peaks with the obtained experimental spectrum measured under similar conditions (see next section), the average shape of the spectra is quite similar, and the position of the Raman peaks is very close to the experimental values (see vertical lines in Figure 2C and Table 3), confirming the high quality of the performed first-principles calculations. Still, some differences can be noted between experimental and calculated values, which might be connected mainly to the optimization of the position of the atoms at the first step of the calculations which slightly changed the size of the cell.

Atomic displacements of the Raman modes were calculated to provide a visualization of the corresponding atom motions. Figure 3 shows an example of the vibrational patterns of the modes with different symmetries, while the displacements for all 30 Raman active modes can be seen in Figure S4. As expected from the phonon DOS analysis, the vibrational patterns are mostly dominated by either Sb (for modes in the spectral range <130 cm^{-1}) or S motions (for modes in the spectral range >130 cm^{-1}). All A_g and B_{2g} modes involve atomic motions parallel to the vertical XZ or (010) plane, while B_{1g} and B_{3g} modes are strictly aligned with the Y axis or [010] crystallographic direction. This will be further used for the development of a methodology for the assessment of the crystallographic orientation of the ribbons of Sb_2S_3. Moreover, a closer look into the modes in the high wavenumber range (>130 cm^{-1}) yields that most of them (14 out of 18 modes) involve vibrations of only one of three non-equivalent sulfur atoms, which can be further used in defect estimations as discussed in the last section of the article.

Experimental identification of the Raman peaks

One of the first points addressed in the matter Raman spectra measurements was related to the selection of suitable measuring conditions in terms of excitation power density. A previous Raman study on natural stibnite (Sb_2S_3) in a micro configuration showed laser induced

Table 2. Refined atomic coordinates, Wyckoff positions, and isotropic temperature factors of the atoms in the asymmetric unit (3 S and 2 Sb)

Name	Element	X	Y	Z	B_{eq}	Wyck.
S(I)	S	0.04869	0.25000	0.87588	1.416	4c
S(II)	S	0.12599	0.75000	0.43748	1.221	4c
S(III)	S	0.20574	0.25000	0.19077	1.714	4c
Sb(I)	Sb	0.02922	0.25000	0.32607	1.478	4c
Sb(II)	Sb	0.14934	0.75000	0.03580	1.795	4c

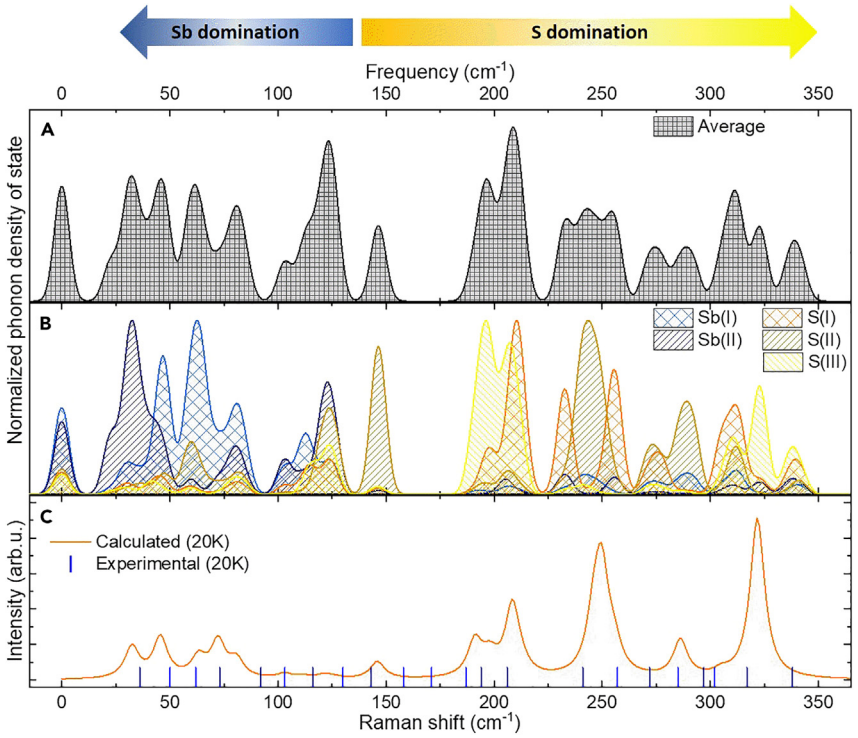

Figure 2. Phonon Density of State (DOS) of Sb_2S_3

(A) Total phonon DOS.

(B) Partial phonon DOS calculated for each non-equivalent atom site.

(C) Calculated Raman scattering spectra. Vertical lines indicate the position of the Raman peaks defined from the experimental spectra measured on the sample cooled down to 20 K.

alterations, which are slightly different from a thermal-induced degradation process, suggesting that stibnite and related compounds are prone to specific photo-degradation effects.[19] In the case of the current study, the optimal excitation power density was found to be around 25 Wcm^{-2} and it was used for all the further experiments (see the method details section for more information about influence of the excitation power density on the Raman spectra of Sb_2S_3). In the further investigations, the experimental position of the Raman peaks has been defined by employing different approaches: multiwavelength Raman study, low temperature measurements, and polarization measurements. The first two measurements were performed on the powder sample to avoid any interference from the crystallographic orientation, while the polarization measurements were performed on the (100) plane of the monocrystalline mineral sample. The resulting spectra from all these measurements are included in Figure 4. It is worth noticing that the multiwavelength approach has already been used for a variety of compounds,[33,43] including low dimensional 2D and 1D materials,[31,44] in order to understand their complex fingerprint Raman spectra consisting of a high number of overlapped peaks.

This study was performed by applying excitation lasers ranging from the near ultraviolet (NUV) to the near infrared (NIR) spectral regions, and several spectral variations can be observed when changing the excitation wavelength allowing a more precise identification of the peaks. Namely, the variations are expressed by clear changes in the relative intensity of some of the peaks. To identify these changes, a fitting function consisting in the deconvolution of individual Lorentzian shaped peaks was performed.

The fitting procedure was carried out on all spectra presented in Figure 4 (an example is given in Figure S5). As a result of the application of this generalized fitting function on all spectra obtained under different excitation wavelengths, a total of 18 peaks were resolved from the multiwavelength Raman study (Table 3). In the method details section, a more detailed discussion on the variations in the Raman spectra measured under different excitations is provided together with an explanation of these changes.

Based on this discussion, it can be concluded that the 632.8 or 785 nm excitation wavelengths are the optimal ones for the Raman analysis of Sb_2S_3, as they are close to resonant conditions which allows the detection of very low amounts of material (e.g., in extremely thin film applications), or revealing the presence of Sb_2S_3 phase as an undesired sub-product in the synthesis of another compound.

Although the deconvolution of most of the peaks was possible from the multiwavelength Raman analysis, in some cases it is still challenging to establish the precise position of the peaks due to their high number and close frequency values. To better resolve the peaks, low temperature (20 K) Raman measurements were performed using a 632.8 nm excitation wavelength. The results are shown in Figure 4C, together with the fitting function employed. As it can be observed, the reduction of the thermal dispersion of the phonon states ($\Gamma 0 + \Delta\Gamma(T)$) decreases the FWHM of the Raman peaks, associated with a blue shift of the peak position due to reduction in thermal agitation of the lattice.

Table 3. Herein, the position of the peaks (experimentally measured and calculated), their FWHM, and the symmetry assignment are collected; together with the optimal excitation wavelength for its detection and a comparison with previously reported bibliography values (experimental and first principles calculations)

	This work			Literature		
				Ref. [21] (cm^{-1})	Ref. [17] (cm^{-1})	
#	λex (nm)	RS experiment [Sym.] (cm^{-1})	RS calculated [Sym.] (cm^{-1})	785 nm	632.8 nm	RS calculated [Sym.]
1		36 [B_{xg}]	31.9 [B_{1g}]		39	47.7 [B_{1g}]
2			32.5 [B_{3g}]			50.8 [B_{3g}]
3	785	50 [A_g]	45.5 [A_g]		50	54.2 [A_g]
4			46.4 [B_{2g}]			46.8 [B_{2g}]
5	785	58 [B_{3g}]	63.1 [B_{3g}]		59	69.0 [B_{3g}]
6			65.1 [B_{1g}]			68.8 [B_{1g}]
7	632.8	71 [A_g]	72.2 [A_g]		71	74.2 [A_g]
8	785	89 [B_{xg}]	80.8 [B_{2g}]			99.1[B_{2g}]
9	632.8	100 [A_g]	102.9 [A_g]		99	100.0 [A_g]
10	632.8	116 [B_{xg}]	111.5 [B_{2g}]			112.1 [B_{2g}]
11	785	125 [B_{xg}]	121.2 [B_{2g}]		125	125.0 [B_{2g}]
12	442	128 [A_g]	125.4 [A_g]			131.5 [A_g]
13		143[a] [B_{xg}]	145.7 [B_{2g}]			171.0 [B_{2g}]
14	785	155 [A_g]	147.0 [A_g]	157	156	169.5 [A_g]
M1		171[a] [MP]				
M2		187[a] [MP]		180	180	
15	785	190 [A_g]	191.0 [A_g]	192	189	197.4 [A_g]
16			195.4 [B_{2g}]			199.5 [B_{2g}]
17			196.8 [B_{1g}]			186.6 [B_{1g}]
18			198.4 [B_{3g}]			198.1 [B_{3g}]
19	785	205 [B_{3g}]	208.4 [B_{3g}]	204	207	200.8 [B_{3g}]
20			212.6 [B_{1g}]			208.2 [B_{1g}]
21			246.1 [B_{1g}]	228	225	229.3 [B_{1g}]
22	785	238 [B_{3g}]	249.8 [B_{3g}]	239	237	231.4 [B_{3g}]
23	355	256 [A_g]	255.5 [A_g]	256	254	251.0 [A_g]
24	355	268 [B_{xg}]	255.6 [B_{2g}]			254.6 [B_{2g}]
25	Any	282 [A_g]	286.2 [A_g]	283	281	261.6 [A_g]
26		297[a] [B_{xg}]	291.9 [B_{2g}]			278.0 [B_{2g}]
27	632.8	300 [A_g]	305.2 [A_g]	304	300	278.0 [A_g]
28			313.0 [B_{2g}]			285.9 [B_{2g}]
29	785	310 [A_g]	321.7 [A_g]	312		290.7[A_g]
30		338[a] [B_{xg}]	323.7 [B_{2g}]			295.5 [B_{2g}]

[a]Peaks resolved only in the spectra measured at 20 K (λ_{ex} = 632.8 nm). See method details for more information about the origin of these peaks.

This allowed a better estimation of the position of the peaks, as well as their relative intensity (see method details section for a more explicit discussion). All the peaks found in the spectra measured at low temperature are collected in Table S1.

Finally, to deepen into the analysis of the fundamental vibrational properties of the Sb_2S_3 compound, polarization measurements were performed on the main plane of the single crystalline mineral sample, allowing assigning the symmetries of the observed Raman peaks. This was done both for the spectra measured in the full spectral range (Figure 4B) and for the spectra measured with a special accessory filters setup for ultra-low frequency measurements (see Figure S6).

As result of the performed analysis of the Raman spectra measured under different conditions, 20 out of 30 possible peaks were resolved and their symmetry was experimentally defined. Most of these peaks have been previously observed from experimental investigations[17,21]; however, several peaks were possible to resolve only when using the different approaches presented in the current work.

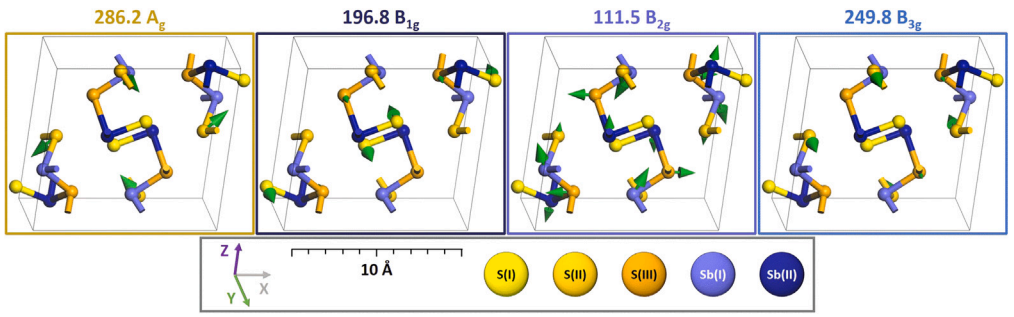

Figure 3. Examples of the atomic displacement of the Raman modes with different symmetries

Raman based methodologies for the assessment of critical properties of Sb_2S_3

It is well-known and has been mentioned in the introduction section that the crystallographic structure of Sb_2S_3 is highly anisotropic, which has a significant impact on its optical and electrical properties depending on the orientation of the ribbons. This becomes more critical when polycrystalline thin films are used in different optoelectronic devices, as it can define their highest and lowest performance. In this regard, having a fast and feasible methodology that also allows in-sample identification of the crystallographic orientation of the ribbons is of outmost importance for the efficient application of the Sb_2S_3 compound in optoelectronic devices.

Expectedly, a strong variation in the crystallographic orientation has a significant impact on the Raman spectra. This can be concluded from the polarized measurements performed previously and arises from the calculated active Raman modes for different crystallographic planes (see Table S2 in supplemental information), corresponding to the cross and parallel orientation of ribbons. This also defines that

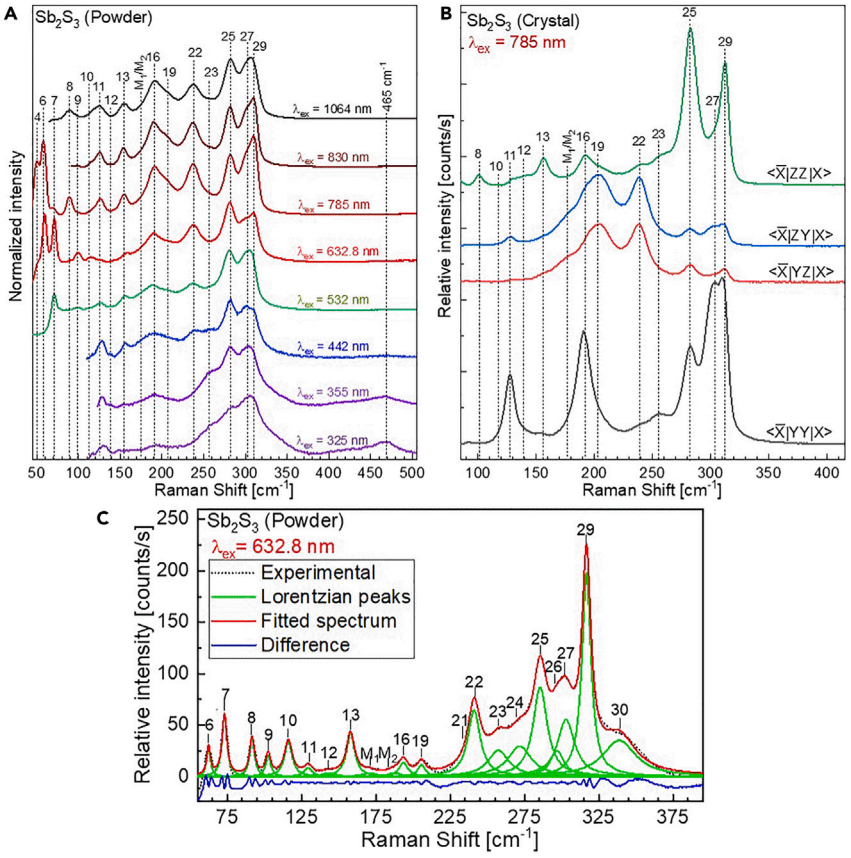

Figure 4. Experimental Raman spectra of Sb_2S_3

(A) Multiwavelength Raman spectra of the Sb_2S_3 powder sample. The spectra are shifted along the Y axis for convenience.

(B) Raman polarization measurements on the Sb_2S_3 crystal under a 785 nm excitation wavelength. The spectra are shifted along the Y axis for convenience.

(C) Fitting of the Raman spectrum of the Sb_2S_3 powder sample measured at a temperature of 20 K with a 632.8 nm excitation wavelength.

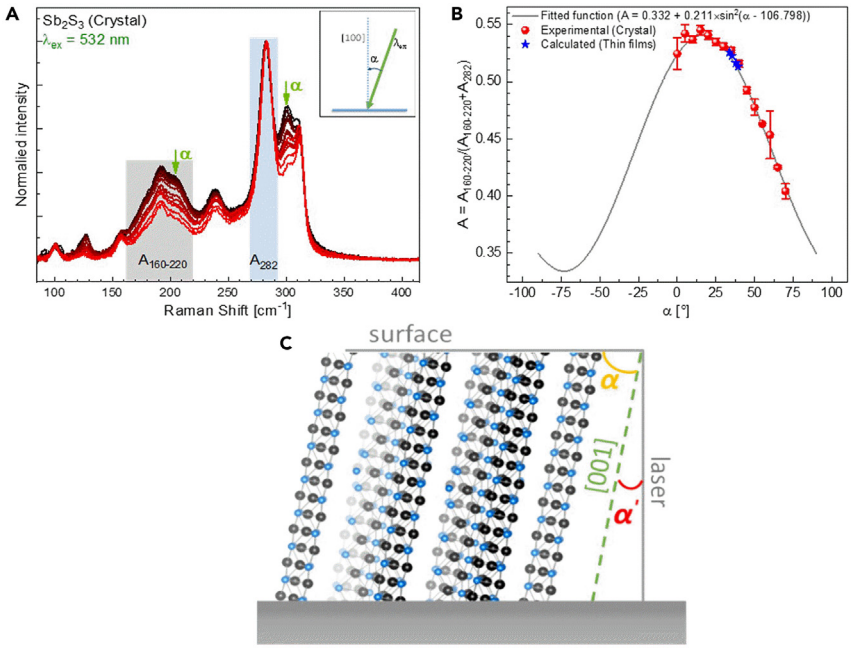

Figure 5. Illustration of the developed Raman-based methodology for assessment of ribbon inclination in Sb_2S_3

(A) Raman spectra measured at different angles between the excitation wavelength and the [100] direction.

(B) Dependence of the relative integrated intensity with the angle α. The fitting function obtained is indicated in the caption. The error bars were obtained as standard deviations of the A value calculated for the spectra measured in different points of the monocrysalline sample.

(C) Schematic view of a thin film with ribbons inclined toward the normal to the surface (also aligned with the direction of the excitation laser beam) on the angle α'.

the atomic displacement (Figures 3 and S3) of the B_{1g} and B_{3g} modes are perpendicular to the (010) plane in which the rest of the modes are vibrating. Taking this into account, Raman scattering spectra were measured on the (100) facet of the single crystalline mineral at different angles between the incident laser beam and the normal of the (100) plane toward the (001) plane, as sketched in Figure S7. The obtained Raman spectra are shown in Figure 5A. Clear changes can be seen in the spectra measured at different angles, namely an increase of the intensity of the peaks around 125, 200, 250, and 300 cm^{-1}.

To quantify the changes observed in the spectra obtained experimentally and, thus, of the overall influence of crystallographic orientation, the integrated intensity of the 160–220 cm^{-1} frequency region was calculated in relation to the integrated intensity of the 282 cm^{-1} peak. Afterward, the dependency of the calculated relative integrated intensity ($A = A_{160\text{-}220}/(A_{160\text{-}220} + A_{182})$) was constructed as a function of the angle in Figure 5B. Considering that the angular dependency of Raman active modes is a squared function involving the polarization vectors of the electric fields of the incident and scattered light,[45] the data obtained experimentally have been fitted using a squared sine function achieving an error of $R_2 = 0.991$ (the solid line in the Figure 5B).

Since in the case of thin films the optimal orientation of the ribbons is perpendicular to the substrate, it is interesting to define the α' angle between the normal to the thin film surface and the ribbons inclination as presented in Figure 5C. The sought-for angle α' correlates with the aforementioned defined angle α as $\alpha' = 90° - \alpha$. Taking this into account, the following formula is obtained for calculating the inclination of the $[Sb_4S_6]_n$ ribbons to the normal to the surface of the sample:

$$\alpha' = -16.80 + \sin^{-1}\left(0.97 \times \sqrt{5.00 \times A - 1.66}\right) \quad \text{(Equation 1)}$$

In order to verify the applicability of the proposed methodology, Raman spectra of Sb_2S_3 of two different thin films were obtained under λ_{ex} = 532 nm (see Figure S8). According to the methodology described previously, the relative integrated intensity of the band in spectral range 160–220 cm^{-1} has been identified (stars in the Figure 5B), resulting in the α' angle to be around 40° (the angle between ribbons and the normal to the thin film surface as a direct result of Equation 1). It should be mentioned that the analysis of the XRD data also did not show significant differences between the measured thin films (see method details for more information), approving their insignificant difference from the structural point of view.

A close look on the spectra measured from the (100) plane of the mineral crystal under different laser beam inclinations (Figure 5A) allows highlighting that the relative intensity of the peak at 100 cm^{-1} is independent from the inclination of the ribbons. The previously calculated atomic displacement for the mode assigned to this peak shows that it involves vibrations of both S and Sb atoms.

On the other hand, as commented before, the most intense Raman peak at 282 cm^{-1} is assigned to the mode which involves vibrations of only S atoms. Taking this into account, it is possible to assume that the change in the relative intensity of these two peaks should correlate with the change in the ratio of S/Sb or, in other words, with amount of point defects in the Sb_2S_3 structure. Additionally, the other two Raman peaks at 300 and 310 cm^{-1} (#27 and #29 in Table 3) are also assigned to the modes that include the vibration of only S anions which makes them also

suitable for the assessment of point defect formation in the Sb_2S_3 structure. Moreover, from the calculated atomic displacements for all three S-related peaks (at 282, 300 and 310 cm^{-1}) it is seen that they involve only one of the sulfur anions in a specific non-equivalent position. In this regard, the change of the relative intensity of only one of these peaks compared to the peak at 100 cm^{-1} will indicate a preferential formation of S-related point defects (sulfur vacancies, substitutions, or interstitials) at a specific non-equivalent position. However, these assumptions still need to be verified by performing the analysis of the Raman spectra from a specific set of samples with different S/Sb ratio.

The presented methodologies and assumptions for the direct application of Raman spectra proves that this spectroscopic technique is a powerful tool for quality control and that it can be implemented for the *in-situ* and in-sample assessment of the crystallographic and structural properties of Sb_2S_3 thin films. Nevertheless, further detailed analyses of specially prepared sets of samples should be used in order to validate the proposed methodology and assumptions. Moreover, as follows from the aforementioned multiwavelength Raman study , there are several variations in the relative intensity of the peaks, which suggest that any possible methodology based on RS should be optimized (e.g., by adjusting the coefficients in Equation 1) for the specific measurement conditions employed.

Conclusions

The present study shows a detailed structural, chemical, and vibrational analysis of Sb_2S_3 powder, single crystalline mineral, and thin film samples. The performed XRD analysis was completed by a Rietveld refinement of the powder diffractogram, yielding a single phase of the powder sample and details about the structural properties of the high quality Sb_2S_3 compound. The EMPA measurements performed in the mineral did not show the presence of any impurities and the chemical composition of the analyzed sample was close to stoichiometric, with insignificant variations between the measured points. The results of the Rietveld refinement were used for the calculation of the lattice dynamics by first-principles. This study provided information about the distribution of the phonon density of states at different wavenumbers and two ranges with dominant Sb and S vibrations were possible to highlight. The atomic displacements for each of the Raman active modes have been analyzed allowing proposing several assumptions for the direct application of RS for the assessment of critical crystallographic and structural properties of Sb_2S_3. The vibrational analysis of all samples was completed by means of an advanced investigation of the Raman spectra. To better resolve all peaks, a multiwavelength Raman study has been performed on the powder sample and completed with the analysis of the spectra at low temperature and analysis of the spectra measured under different polarization conditions in the single crystalline mineral. As result, 20 out of the 30 theoretically predicted peaks have been clearly resolved in the measured spectra. Additionally, the Raman study included the identification of optimal measurement conditions regarding the excitation power density and excitation wavelength. The first was found to result in formation Sb_2O_3 secondary phase when exceeding the proper power density, and for the latter two laser lines close to resonant condition (632.8 and 785 nm) showed the highest signal-to-noise ratio. This opens the door to detecting small quantities of this material, for example in thin film research field, or to improve its detection if behaving as an undesired phase. Finally, based on the calculated atomic displacements and analysis of the Raman tensors a methodology was proposed for the identification of the crystallographic orientation of the ribbons, and an assumption was made about the possible influence of the point defects concentration on the relative intensity of specific Raman peaks. This opens the possibility for exploiting RS as a fast, non-destructive, non-invasive technique for assessing the crystallographic orientation and defects in Sb_2S_3 thin films with high lateral resolution.

Limitations of the study

As follows from the performed multiwavelength Raman study, there are several variations in the relative intensity of the peaks, which suggest that any possible methodology based on RS should be optimized (e.g., by adjusting the coefficients in Equation 1) for the specific measurement conditions employed. At the same time the methodologies should be optimized based on the equipment that is employed during the measurements.

STAR★METHODS

Detailed methods are provided in the online version of this paper and include the following:

- KEY RESOURCES TABLE
- RESOURCE AVAILABILITY
  - Lead contact
  - Materials availability
  - Data and code availability
- METHOD DETAILS
  - Samples description
  - Instrumental setup
  - Lattice dynamics calculations
  - Study of excitation power density
  - Discussion on the identified Raman features
  - Analysis of the Sb_2S_3 thin films

SUPPLEMENTAL INFORMATION

Supplemental information can be found online at https://doi.org/10.1016/j.isci.2024.109619.

ACKNOWLEDGMENTS

This work is part of the R + D + i MaterOne project Ref. PID 2020-116719RB-C42 funded by MCIN/AEI/10.13039/5011000110033. Authors from IREC belong to the MNT-Solar Consolidated Research Group of the "Generalitat de Catalunya" (ref. 2021 SGR 01286) and are grateful to European Regional Development Funds (ERDF, FEDER Programa Competitivitat de Catalunya 2007–2013). V.R. acknowledges the support of the predoctoral program AGAUR-FI ajuts (2023 FI-1 00436) Joan Oró of the Secretariat of Universities and Research of the Department of Research and Universities of the Generalitat of Catalonia and the European Social Plus Fund. M.G. acknowledges the financial support from MCIN/AEI/10.13039/501100011033 and from FSE+ in the framework of Ramon y Cajal fellowship (RYC2022-035588-I). This project has received funding from the European Union's Horizon 2020 research and innovation programme under Marie Skłodowska-Curie GA No. 801342 (Tecniospring INDUSTRY) and the Government of Catalonia's Agency for Business Competitiveness (ACCIÓ).

AUTHOR CONTRIBUTIONS

V.R.: writing – original draft, investigation, formal analysis, visualization, data curation, methodology; P.V.-F.: writing – review & editing, methodology, conceptualization, validation; X.A.: writing – review & editing, investigation, formal analysis; T.J.: writing – review & editing, investigation; A.L.-G.: writing – review & editing, investigation; A.P.-R.: writing – review & editing, validation, funding acquisition, resources; I.B.-R.: writing – review & editing, validation; V.I.-R.: writing – review & editing, conceptualization, validation, methodology, supervision, project administration; M.G.: writing – review & editing, conceptualization, validation, methodology, supervision, data curation.

DECLARATION OF INTERESTS

The authors declare no competing interests.

Received: January 11, 2024
Revised: March 22, 2024
Accepted: March 26, 2024
Published: March 29, 2024

REFERENCES

1. Yang, M., Fan, Z., Du, J., Li, R., Liu, D., Zhang, B., Feng, K., Feng, C., and Li, Y. (2022). Tailoring the Crystallographic Orientation of a Sb_2S_3Thin Film for Efficient Photoelectrochemical Water Reduction. ACS Catal. *12*, 8175–8184. https://doi.org/10.1021/acscatal.2c01384.
2. Choi, Y.C., Lee, D.U., Noh, J.H., Kim, E.K., and Seok, S.I. (2014). Highly improved Sb_2S_3 sensitized-inorganic-organic heterojunction solar cells and quantification of traps by deep-level transient spectroscopy. Adv. Funct. Mater. *24*, 3587–3592. https://doi.org/10.1002/adfm.201304238.
3. Kondrotas, R., Chen, C., and Tang, J. (2018). Sb_2S_3 Solar Cells. Joule *2*, 857–878. https://doi.org/10.1016/j.joule.2018.04.003.
4. Liu, H., He, Y., Cao, K., Wang, S., Jiang, Y., Liu, X., Huang, K.J., Jing, Q.S., and Jiao, L. (2021). Stimulating the Reversibility of Sb_2S_3 Anode for High-Performance Potassium-Ion Batteries. Small *17*, 2008133. https://doi.org/10.1002/smll.202008133.
5. Wang, T., Shen, D., Liu, H., Chen, H., Liu, Q., and Lu, B. (2020). A Sb_2S_3 Nanoflower/MXene Composite as an Anode for Potassium-Ion Batteries. ACS Appl. Mater. Interfaces *12*, 57907–57915. https://doi.org/10.1021/acsami.0c18285.
6. Delaney, M., Zeimpekis, I., Lawson, D., Hewak, D.W., and Muskens, O.L. (2020). A New Family of Ultralow Loss Reversible Phase-Change Materials for Photonic Integrated Circuits: Sb_2S_3 and Sb_2Se_3. Adv. Funct. Mater. *30*, 2002447. https://doi.org/10.1002/adfm.202002447.
7. Cai, Z., Dai, C.M., and Chen, S. (2020). Intrinsic Defect Limit to the Electrical Conductivity and a Two-Step p-Type Doping Strategy for Overcoming the Efficiency Bottleneck of Sb_2S_3-Based Solar Cells. Sol. RRL *4*, 1900503. https://doi.org/10.1002/solr.201900503.
8. Deng, H., Yuan, S., Yang, X., Cai, F., Hu, C., Qiao, K., Zhang, J., Tang, J., Song, H., and He, Z. (2017). Efficient and stable TiO_2/Sb_2S_3 planar solar cells from absorber crystallization and Se-atmosphere annealing. Mater. Today Energy *3*, 15–23. https://doi.org/10.1016/j.mtener.2017.02.001.
9. Lin, J., Mahmood, A., Chen, G., Ahmad, N., Chen, M., Fan, P., Chen, S., Tang, R., and Liang, G. (2022). Crystallographic orientation control and defect passivation for high-efficient antimony selenide thin-film solar cells, Mater. Today Phys. *27*, 100772. https://doi.org/10.1016/j.mtphys.2022.100772.
10. Arun, P., and Vedeshwar, A.G. (1996). On the structure of stibnite (Sb_2S_3). J. Mater. Sci. *31*, 6507–6510. https://doi.org/10.1007/BF00356255.
11. Shaji, S., Arato, A., O'Brien, J.J., Liu, J., Castillo, G.A., Palma, M.I.M., Roy, T.K.D., and Krishnan, B. (2010). Chemically deposited Sb_2S_3 thin films for optical recording. J. Phys. D Appl. Phys. *43*, 075404. https://doi.org/10.1088/0022-3727/43/7/075404.
12. Perales, F., Heras, C.d.l., Agulló-Rueda, G.,F., and Agulló-Rueda, F. (2007). Optical and structural properties in the amorphous to polycrystalline transition in Sb_2S_3 thin films. J. Phys. D Appl. Phys. *40*, 2440–2444. https://doi.org/10.1088/0022-3727/40/8/005.
13. Ben Nasr, T., Maghraoui-Meherzi, H., Ben Abdallah, H., and Bennaceur, R. (2011). Electronic structure and optical properties of Sb_2S_3 crystal. Phys. B Condens. Matter *406*, 287–292. https://doi.org/10.1016/j.physb.2010.10.070.
14. Haj Lakhdar, M., Ouni, B., and Amlouk, M. (2014). Dielectric relaxation, modulus behavior and conduction mechanism in Sb_2S_3 thin films. Mater. Sci. Semicond. Process. *19*, 32–39. https://doi.org/10.1016/j.mssp.2013.11.038.
15. Koc, H., Mamedov, A.M., Deligoz, E., and Ozisik, H. (2012). First principles prediction of the elastic, electronic, and optical properties of Sb_2S_3 and Sb_2Se_3 compounds. Solid State Sci. *14*, 1211–1220. https://doi.org/10.1016/j.solidstatesciences.2012.06.003.
16. Avilez Garcia, R.G., Meza Avendaño, C., Pal, M., Paraguay Delgado, F., and Mathews, N.R. (2016). Antimony sulfide (Sb_2S_3) thin films by pulse electrodeposition: Effect of thermal treatment on structural, optical and electrical properties. Mater. Sci. Semicond. Process. *44*, 91–100. https://doi.org/10.1016/j.mssp.2015.12.018.
17. Liu, Y., Chua, K.T.E., Sum, T.C., and Gan, C.K. (2014). First-principles study of the lattice dynamics of Sb_2S_3. Phys. Chem. Chem. Phys. *16*, 345–350. https://doi.org/10.1039/c3cp53879f.
18. Parize, R., Cossuet, T., Chaix-Pluchery, O., Roussel, H., Appert, E., and Consonni, V. (2017). *In situ* analysis of the crystallization process of Sb_2S_3 thin films by Raman scattering and X-ray diffraction. Mater. Des. *121*, 1–10. https://doi.org/10.1016/j.matdes.2017.02.034.
19. Makreski, P., Petruševski, G., Ugarković, S., and Jovanovski, G. (2013). Laser-induced transformation of stibnite (Sb_2S_3) and other structurally related salts. Vib. Spectrosc. *68*, 177–182. https://doi.org/10.1016/j.vibspec.2013.07.007.
20. Ibáñez, J., Sans, J.A., Popescu, C., López-Vidrier, J., Elvira-Betanzos, J.J., Cuenca-Gotor, V.P., Gomis, Ó., Manjón, F.J., Rodríguez-Hernández, P., and Muñoz, A. (2016). Structural, Vibrational, and Electronic Study of Sb_2S_3 at High Pressure. J. Phys. Chem. C *120*, 10547–10558. https://doi.org/10.1021/acs.jpcc.6b01276.

21. Kharbish, S., Libowitzky, E., and Beran, A. (2009). Raman spectra of isolated and interconnected pyramidal XS3 groups (X = Sb,Bi) in stibnite, bismuthinite, kermesite, stephanite and bournonite. Eur. J. Mineral *21*, 325–333. https://doi.org/10.1127/0935-1221/2009/0021-1914.
22. Juárez, B.H., Rubio, S., Sánchez-Dehesa, J., and López, C. (2002). Antimony Trisulfide Inverted Opals: Growth, Characterization, and Photonic Properties. Adv. Mater. *14*, 1486–1490. https://doi.org/10.1002/1521-4095(20021016)14:20<1486::AID-ADMA1486>3.0.CO;2-P.
23. Fleck, N., Hobson, T.D.C., Savory, C.N., Buckeridge, J., Veal, T.D., Correia, M.R., Scanlon, D.O., Durose, K., and Jäckel, F. (2020). Identifying Raman modes of Sb_2Se_3 and their symmetries using angle-resolved polarised Raman spectra. J. Mater. Chem. A *8*, 8337–8344. https://doi.org/10.1039/d0ta01783c.
24. Gutiérrez, Y., Ovvyan, A.P., Santos, G., Juan, D., Rosales, S.A., Junquera, J., García-Fernández, P., Dicorato, S., Giangregorio, M.M., Dilonardo, E., et al. (2022). Interlaboratory study on Sb_2S_3 interplay between structure, dielectric function, and amorphous-to-crystalline phase change for photonics. iScience *25*, 104377. https://doi.org/10.1016/j.isci.2022.104377.
25. (2023). RUFF Database Stibnite R120137. https://rruff.info/stibnite/display=default/R120137.
26. Park, S.N., Kim, S.Y., Lee, S.J., Sung, S.J., Yang, K.J., Kang, J.K., and Kim, D.H. (2019). Controlled synthesis of (*hk*1) preferentially oriented Sb_2Se_3 rod arrays by co-evaporation for photovoltaic applications. J. Mater. Chem. *7*, 25900–25907. https://doi.org/10.1039/C9TA08289A.
27. Guc, M., Hariskos, D., Calvo-Barrio, L., Jackson, P., Oliva, F., Pistor, P., Perez-Rodriguez, A., and Izquierdo-Roca, V. (2017). Resonant Raman scattering based approaches for the quantitative assessment of nanometric ZnMgO layers in high efficiency chalcogenide solar cells. Sci. Rep. *7*, 1144. https://doi.org/10.1038/s41598-017-01381-4.
28. Fairbrother, A., Izquierdo-Roca, V., Fontané, X., Ibáñez, M., Cabot, A., Saucedo, E., and Pérez-Rodríguez, A. (2014). ZnS grain size effects on near-resonant Raman scattering: optical non-destructive grain size estimation. CrystEngComm *16*, 4120–4125. https://doi.org/10.1039/C3CE42578A.
29. Lu, X., Utama, M.I.B., Lin, J., Gong, X., Zhang, J., Zhao, Y., Pantelides, S.T., Wang, J., Dong, Z., Liu, Z., et al. (2014). Large-Area Synthesis of Monolayer and Few-Layer $MoSe_2$ Films on SiO_2 Substrates. Nano Lett. *14*, 2419–2425. https://doi.org/10.1021/nl5000906.
30. Zhang, Y., Zhang, Y., Ji, Q., Ju, J., Yuan, H., Shi, J., Gao, T., Ma, D., Liu, M., Chen, Y., et al. (2013). Controlled Growth of High-Quality Monolayer WS_2 Layers on Sapphire and Imaging Its Grain Boundary. ACS Nano *7*, 8963–8971. https://doi.org/10.1021/nn403454e.
31. Placidi, M., Dimitrievska, M., Izquierdo-Roca, V., Fontané, X., Castellanos-Gomez, A., Pérez-Tomás, A., Mestres, N., Espindola-Rodriguez, M., López-Marino, S., Neuschitzer, M., et al. (2015). Multiwavelength excitation Raman scattering analysis of bulk and two-dimensional MoS_2: vibrational properties of atomically thin MoS_2 layers. 2D Mater. *2*, 035006. https://doi.org/10.1088/2053-1583/2/3/035006.
32. Dimitrievska, M., Oliva, F., Guc, M., Giraldo, S., Saucedo, E., Pérez-Rodríguez, A., and Izquierdo-Roca, V. (2019). Defect characterisation in $Cu_2ZnSnSe_4$ kesterites *via* resonance Raman spectroscopy and the impact on optoelectronic solar cell properties. J. Mater. Chem. A *7*, 13293–13304. https://doi.org/10.1039/C9TA03625C.
33. Garcia-Llamas, E., Guc, M., Bodnar, I.V., Fontané, X., Caballero, R., Merino, J.M., León, M., and Izquierdo-Roca, V. (2017). Multiwavelength excitation Raman scattering of $Cu_2ZnSn_{1-x}Ge_x(S,Se)_4$ single crystals for earth abundant photovoltaic applications. J. Alloys Compd. *692*, 249–256. https://doi.org/10.1016/j.jallcom.2016.09.035.
34. Guc, M., Andrade-Arvizu, J., Ahmet, I.Y., Oliva, F., Placidi, M., Alcobé, X., Saucedo, E., Pérez-Rodríguez, A., Johnson, A.L., and Izquierdo-Roca, V. (2020). Structural and vibrational properties of α- and π-SnS polymorphs for photovoltaic applications. Acta Mater. *183*, 1–10. https://doi.org/10.1016/j.actamat.2019.11.016.
35. Pistor, P., Meyns, M., Guc, M., Wang, H.C., Marques, M.A., Alcobé, X., Cabot, A., and Izquierdo-Roca, V. (2020). Advanced Raman spectroscopy of $Cs_2AgBiBr_6$ double perovskites and identification of $Cs_3Bi_2Br_9$ secondary phases. Scripta Mater. *184*, 24–29. https://doi.org/10.1016/j.scriptamat.2020.03.040.
36. Guc, M., Oliva, F., Fairbrother, A., Jawhari, T., Alcobe, X., Placidi, M., Pérez-Rodríguez, A., Saucedo, E., and Izquierdo-Roca, V. (2020). Cu-Sn-S system: Vibrational properties and coexistence of the Cu_2SnS_3, Cu_3SnS_4 and Cu_4SnS_4 compounds. Scripta Mater. *186*, 180–184. https://doi.org/10.1016/j.scriptamat.2020.05.050.
37. Vidal-Fuentes, P., Guc, M., Becerril-Romero, I., Sylla, D., Alcobé, X., Sánchez, Y., Pérez-Rodríguez, A., Saucedo, E., and Izquierdo-Roca, V. (2021). Insights on the Thermal Stability of the Sb_2Se_3 Quasi-1D Photovoltaic Technology. Sol. RRL *5*, 2100517. https://doi.org/10.1002/solr.202100517.
38. Schorr, S., Gurieva, G., Guc, M., Dimitrievska, M., Pérez-Rodríguez, A., Izquierdo-Roca, V., Schnohr, C.S., Kim, J., Jo, W., and Merino, J.M. (2020). Point defects, compositional fluctuations, and secondary phases in non-stoichiometric kesterites. JPhys Energy *2*, 012002. https://doi.org/10.1088/2515-7655/ab4a25.
39. Guc, M., Bailo, E., Fonoll-Rubio, R., Atlan, F., Placidi, M., Jackson, P., Hariskos, D., Alcobe, X., Pistor, P., Becerril-Romero, I., et al. (2022). Evaluation of defect formation in chalcopyrite compounds under Cu-poor conditions by advanced structural and vibrational analyses. Acta Mater. *223*, 117507. https://doi.org/10.1016/j.actamat.2021.117507.
40. Atlan, F., Becerril-Romero, I., Giraldo, S., Rotaru, V., Sánchez, Y., Gurieva, G., Schorr, S., Arushanov, E., Pérez-Rodríguez, A., Izquierdo-Roca, V., and Guc, M. (2023). Stability of $Cu_2ZnSnSe_4$/CdS heterojunction based solar cells under soft post-deposition thermal treatments. Sol. Energy Mater. Sol. Cells *249*, 112046. https://doi.org/10.1016/j.solmat.2022.112046.
41. Bayliss, P., and Nowacki, W. (1972). Refinement of the crystal structure of stibnite. Sb_2S_3, Z. Kristallogr. - Cryst. Mater. *135*, 308–315. https://doi.org/10.1524/zkri.1972.135.3-4.308.
42. Efthimiopoulos, I., Buchan, C., and Wang, Y. (2016). Structural properties of Sb_2S_3 under pressure: evidence of an electronic topological transition. Sci. Rep. *6*, 24246. https://doi.org/10.1038/srep24246.
43. Dimitrievska, M., Xie, H., Fairbrother, A., Fontané, X., Gurieva, G., Saucedo, E., Pérez-Rodríguez, A., Pérez-Rodríguez, A., and Izquierdo-Roca, V. (2014). Multiwavelength excitation Raman scattering of $Cu_2ZnSn(S_xSe_{1-x})_4$ ($0 \leq x \leq 1$) polycrystalline thin films: Vibrational properties of sulfoselenide solid solutions. Appl. Phys. Lett. *105*, 031913. https://doi.org/10.1063/1.4891333.
44. Vidal-Fuentes, P., Guc, M., Alcobe, X., Jawhari, T., Placidi, M., Pérez-Rodríguez, A., Saucedo, E., and Roca, V.I. (2019). Multiwavelength excitation Raman scattering study of Sb_2Se_3 compound: fundamental vibrational properties and secondary phases detection. 2D Mater. *6*, 045054. https://doi.org/10.1088/2053-1583/ab4029.
45. Loudon, R. (1965). Theory of the resonance Raman effect in crystals. J. Phys. *26*, 677–683. https://doi.org/10.1051/jphys:019650026011067700.
46. Rietveld, H.M. (1969). A profile refinement method for nuclear and magnetic structures. J. Appl. Crystallogr. *2*, 65–71. https://doi.org/10.1107/S0021889869006558.
47. Coelho, A.A., Evans, J., Evans, I., Kern, A., and Parsons, S. (2011). The TOPAS symbolic computation system. Powder Diffr. *26*, S22–S25. https://doi.org/10.1154/1.3661087.
48. Cheary, R.W., Coelho, A.A., and Cline, J.P. (2004). Fundamental Parameters Line Profile Fitting in Laboratory Diffractometers. J. Res. Natl. Inst. Stand. Technol. *109*, 1–25. https://doi.org/10.6028/jres.109.002.
49. Perdew, J.P., Ruzsinszky, A., Constantin, L.A., Sun, J., Csonka, G.I., Constantin, L.A., Zhou, X., and Burke, K. (2009). Some Fundamental Issues in Ground-State Density Functional Theory: A Guide for the Perplexed. Phys. Rev. Lett. *5*, 902–908. https://doi.org/10.1021/ct800531s.
50. Clark, S.J., Segall, M.D., Pickard, C.J., Hasnip, P.J., Probert, M.I.J., Refson, K., and Payne, M.C. (2005). First principles methods using CASTEP. Z. für Kristallogr. - Cryst. Mater. *220*, 567–570. https://doi.org/10.1524/zkri.220.5.567.65075.
51. Shongalova, A., Correia, M.R., Vermang, B., Cunha, J.M.V., Salomé, P.M.P., and Fernandes, P.A. (2018). On the identification of Sb_2Se_3 using Raman scattering. MRS Commun. *8*, 865–870. https://doi.org/10.1557/mrc.2018.94.
52. Johnson, B.B., and Peticolas, W.L. (1976). The Resonant Raman Effect. Annu. Rev. Phys. Chem. *27*, 465–521. https://doi.org/10.1146/annurev.pc.27.100176.002341.
53. Yu, P.Y., and Cardona, M. (2010). Fundamentals of Semiconductors (Springer Berlin). https://doi.org/10.1007/b137661.
54. Zeng, H., Cai, W., Cao, B., Hu, J., Li, Y., and Liu, P. (2006). Surface Optical Phonon Raman Scattering in Zn/ZnO Core-Shell Structured Nanoparticles. Appl. Phys. Lett. *88*, 181905. https://doi.org/10.1063/1.2199968.
55. Gupta, R., Xiong, Q., Mahan, G.D., and Eklund, P.C. (2003). Laser-Induced Fano Resonance Scattering in Silicon Nanowires. Nano Lett. *3*, 1745–1750. https://doi.org/10.1021/nl0341133.

STAR★METHODS

KEY RESOURCES TABLE

REAGENT or RESOURCE	SOURCE	IDENTIFIER
Chemicals, peptides, and recombinant proteins		
Mineral Sb_2S_3 Single Crystal	Personal Collection	N/A
Sb shots	Alfa Aesar	CAS: 7440-36-0
Sulfur	Alfa Aesar	CAS: 7704-34-9
Software and algorithms		
Origin 2018	Origin Lab Corporation	www.originlab.com
CASTEP	Clark et al.[50]	www.castep.org
TOPAS v6	Coelho et al.[47]	www.bruker.com

RESOURCE AVAILABILITY

Lead contact

Further information and requests for resources and materials should be directed to and will be fulfilled by the lead contact, Maxim Guc. e-mail: mguc@irec.cat.

Materials availability

This study did not generate new unique reagents.

Data and code availability

- All data reported in this article is available upon reasonable request from the lead contact.
- This study does not report any original code.
- Any additional information required to reanalyze the data reported in this paper is available from the lead contact upon reasonable request.

METHOD DETAILS

Samples description

This study combines a detailed structural and vibrational analysis of the Sb_2S_3 compound performed on different types of samples which are described below.

A natural single crystalline mineral sample of Sb_2S_3 (Stibnite) with dimensions of about 3 × 2 × 1 cm^3 and clear facets (Figure S1) was employed for the present study. The purity of the sample was studied by XRD and microprobe analyses to ensure its composition and quality.

In addition, to avoid the influence of the crystallographic orientation of the single crystalline mineral during its characterization with different techniques, a randomly oriented micro crystalline powder sample of Sb_2S_3 was fabricated by agate mortar from a small piece of about 2 × 2 × 2 mm^3 from the mineral crystal sample through mechanical milling. The milling time was set to 5 min that resulted in a powder sample with no or insignificant preferred crystallographic orientations, as proved by XRD analysis.

Finally, thin film samples of Sb_2S_3 were synthesized on top of an FTO-coated glass substrate (Merck; R_{sh} = 8 Ω sq^{-1}) by a sequential process. Firstly, a Sb metallic precursor layer of 200 nm was deposited by e-beam evaporation (Oerlikon UNIVEX 250) using Sb shots (Alfa Aesar; 1–3 mm, Puratronic, 6N metal basis) in a 4 cc alumina liner. The deposition was conducted in high vacuum with a base vacuum of 10^{-5} mbar and with no intentional substrate heating at a deposition rate of 10 Å/s, controlled by a crystal quartz sensor, the total time elapsed is 200 s + 60 s of pre-conditioning of the target material. Afterward, the layers were introduced in a graphite box with 500 mg of sulfur (Alfa Aesar, Puratronic, 5N metal basis) and were subjected to a reactive annealing process in a tubular furnace, the temperature was raised at 20°C/min and kept at 300°C (for sample A) and 375°C (for sample B) with a dwell time of 30 min, the pressure was kept at 800 mbar (static) defined by an inert argon atmosphere, the furnace was left to cool to room temperature naturally, allowing the formation of Sb_2S_3 layers. The thicknesses and chemical composition of the Sb_2S_3 thin films were determined with an X-ray fluorescence spectrometer Fischerscope XVD. The measurements were conducted in a 4 × 4 point grid covering the full area of the sample using a 50 kV accelerating voltage, an Ni10 filter to reduce background signal, and an integration time per measuring point of 45 s. As a result, the thickness of the Sb_2S_3 thin films were proven to be of 400 nm, and the chemical composition of both samples was close to stoichiometric.

Instrumental setup

Raman measurements were performed in back scattering configuration by using eight excitation wavelengths raging from the near ultraviolet (NUV) up to the near infrared (NIR) spectral regions. The measurements in the NUV and visible regions were carried out using a Raman setup based on a Horiba Jobin Yvon FHR640 monochromator coupled with a deep-cooled CCD detector. The measurements in the NIR were carried out using a Raman setup based on a Horiba Jobin Yvon iHR320 monochromator coupled with a near infrared enhanced CCD detector (for the 785 and 830 nm excitations) or with a deep-cooled InGaAs detector (for the 1064 nm excitation). For each laser, a suitable diffraction grating was chosen: 2400 L/m for 325, 355 and 442 nm; 1800 L/m for 532 nm; 1200 L/m for 632.8, 785 and 830 nm; and 600 L/m for 1064 nm. As a result, a FWHM of the main peak of monocrystalline silicon at 520 cm^{-1} in the range of 5–7 cm^{-1} was obtained for all lasers, allowing the achievement of a relatively high resolution of the spectra measured under different excitation wavelengths. The spectral position of the measurements was calibrated using the same main peak of monocrystalline Si at 520 cm^{-1}. The excitation laser was un-polarized and focused on the sample surface on a macro-spot with a diameter in the range of 50–70 μm through a metallographic Olympus objective with ×20 magnification. In the case of the crystal and powder Sb_2S_3 samples, at least three different points were measured under each measuring conditions. As for the Sb_2S_3 thin films up to 16 points were measured in each sample. Low temperature measurements (20 K) were carried out using a close cycle Helium cryostat. To perform the rotation studies, the crystal sample was held by a micrometric actuated angle rotation platform, where the angle was varied between the normal to the (100) surface and the laser beam from 0° to 70°.

In addition, polarization Raman measurements were performed using a LabRam HR800-UV Horiba Jobin Yvon spectrometer in backscattering configuration. A solid-state laser (785 nm wavelength) was used as excitation source in this case. Standard polarization filters were used for polarization measurements and an ultralow frequency notch filter was used for the measurements close to the excitation laser wavelength.

Two types of XRD measurements were performed: on monograin powder and on the crystal samples. For the monograin powder, the powder material was mounted in a cylindrical cavity (15 mm of diameter and 0.15 mm of height) of a silicon single crystal zero background sample holder. A powder diffractogram was obtained in a PANalytical X'Pert PRO MPD Bragg-Brentano powder diffractometer equipped with a Cu tube operating at 45 kV and 40 mA, a Ge (111) Johansson type primary focalizing monochromator and a PIXcel^{1D} detector. High resolution, high statistics, full angular range, Cu $K_{\alpha 1}$ (λ = 1.5406 Å) data were obtained through a $2\theta/\theta$ scan from 4 to 145° 2θ with a step size 0.013° and a measuring time per step of 200 s (PIXcel^{1D} detector: active length = 3.347°) performing three consecutive repeated scans with total measuring time 7.2 h. A full profile analysis, Rietveld method,[46] was applied to the data obtained. The refinements were performed using the TOPAS v6 software.[47] The background was modeled with a 16th order Chebyschev polynomial. The instrumental contribution to the diffraction profile was calculated with the Fundamental Parameters Approach.[48] For the XRD analysis of the crystal sample, the original crystal of Sb_2S_3 was directly mounted in the sample position of the goniometer with its biggest surface matching the diffraction plane. A diffractogram was obtained in a PANalytical X'Pert PRO MPD Bragg-Brentano powder diffractometer using iron filtered Co $K\alpha_{1+2}$ radiation (λ = 1.7903 Å), at 40 kV and 45 mA, and a 1D silicon strip X'Celeretor detector. A standard $2\theta/\theta$ scan was obtained from 5 to 95 degrees of 2θ with step size of 0.013° and a measuring time per step of 2 s (X'Celerator detector: active length = 2.122°). This measurement was performed to determine the crystallographic orientation of the Sb_2S_3 mineral and to confirm its single crystallinity.

Finally, to determine the composition of the Sb_2S_3 mineral, wavelength dispersive X-ray measurements (WDX) were performed using an electron microprobe analysis (EMPA) system (JEOL-JXA 8200) with an energy of 20 keV. In order to obtain reliable results from the WDX measurements, the system was calibrated using elemental standards. A high accuracy of the composition parameters was achieved by averaging over several local measurement points to an integral chemical composition with an accuracy of ±1 at%.

Lattice dynamics calculations

First-principles calculations of the electronic ground state of Sb_2S_3 were performed within the local density approximation using Perdew-Burke-Ernzerhof functional revised for solids,[49] as implemented in the CASTEP code.[50] The cutoff energy for the plane wave basis was set to 600 eV. A self-consistent field (SCF) tolerance better than 10^{-9} eV per atom and a phonon SCF threshold of 10^{-8} eV per atom were imposed. Prior to performing the calculations, the structure was relaxed so that forces on the atoms reached the equilibrium position, and the residual stress was below 3 MPa. Experimentally determined lattice parameters were used as starting point. An integration over the Brillouin zone was performed over a 3 × 3 × 2 Monkhorst-Pack grid in reciprocal space.

Study of excitation power density

As described in the instrumental setup section above, the system used for most of the measurements of Raman spectra can be considered as having a macro configuration due to the relatively large measurement spot size (~70 μm), which therefore results in relatively low excitation power densities. Still, in the Raman spectra of the Sb_2S_3 powder measured under the 532 nm excitation wavelength with various laser power densities (see Figure S9), the appearance of the α-Sb_2O_3 characteristic peaks[51] at 118, 188, 252, 372 and 448 cm^{-1} occurs at a relatively low laser power density of 90 Wcm^{-2}. The relative intensity of these peaks increases continuously with the further increase of the laser power density. In addition, by taking a closer look on the spectra measured with 51 and 70 Wcm^{-2}, it can be observed an increased width of the Raman peaks, which is related to the slight heating of the sample. Based on this, to avoid laser-induced modifications of the samples, laser power densities were kept around 25 Wcm^{-2} for all measurements of all sample types used in the present study.

Discussion on the identified Raman features

When comparing the spectra obtained at different laser excitation wavelengths (Figure 4), it can be observed that the Raman spectra measured under 632.8, 785 and 830 nm excitations exhibit higher signal-to-noise ratio. This is related to the proximity of this wavelength to resonance conditions, and it is due to the coupling of the incident photon energy with the band gap energy of the material.[44] Considering that the reported band gap energy of Sb_2S_3 is close to 1.70 eV[13], the expected resonance effect should occur between 632.8 and 785 nm excitations that correspond to photon energies of 1.95 and 1.58 eV, respectively. However, it can be seen in Figure 4A that approaching the resonance conditions does not have a significant influence on the Raman spectrum from the point of view of relative peak intensities or, in other words, from the point of view of the general shape of Raman spectrum of the Sb_2S_3 compound. This is related to the specific structure of Sb_2S_3 and the non-equivalent position of the atoms in the unit cell, which prevents the appearance of polar modes (or LO-TO splitting effect), and as a result no longitudinal optical component of Raman modes appear in the spectra. The absence of these components, which are known to exhibit the strongest Fröhlich electron–phonon interaction,[52,53] also results in the absence of multiphonon modes, which are barely seen in the spectra measured close to resonance conditions. Taking this into account, it can be concluded that the 632.8 or 785 nm excitation wavelengths are the optimal ones that do not result in significant spectra distortion and allow detecting low amounts of material, for example in thin film applications, or revealing the presence of Sb_2S_3 phase as an undesired sub-product of the synthesis of another compound.

An important spectral feature appears in the Raman spectra measured under NUV excitation (λ_{ex} = 325 and 355 nm), where the presence of a broad, almost Gaussian shaped peak complicates the resolution of most of the individual peaks. Additionally, a broad band at 465 cm^{-1} is present in these two NUV Raman spectra and could not be seen in any other spectra or previously published reports. The detection of the mentioned band was not noted while performing an excitation power density study (Figure S9). However, a more specific degradation under NUV excitation could be related to the photon energy being higher than bond energy of atoms in Sb_2S_3 leading to the formation of amorphous S. A similar effect has been previously reported for the Sb_2Se_3 compound, where the formation of an amorphous Se phase has been detected for any, even the lowest power density of a 325 nm excitation wavelength.[44] To confirm this, a Raman study on pure amorphous S should be performed, although, no such reports were published to the best of our knowledge. It is worth mentioning that some other effects such as resonance with electronic levels above the bandgap, internal structural point defects, surface related optical phonons and/or appearance of the non-centrosymmetric phonon modes can be responsible for the presence of the broad Raman band at 465 cm^{-1} in the spectra measured under NUV excitation, and this should be a matter of further more extensive studies.[17,38,53–55]

From the low temperature measurements (Figure 4B) a better resolution of the peaks in the spectral range 170–210 cm^{-1} is obtained, with 4 peaks being distinguished at 171, 187, 194 and 206 cm^{-1}, when only a broad band (decomposed into peaks at 175, 190 and 205 cm^{-1}) was observed under any excitation wavelength at room temperature. Similarly, the peaks around 100 and 250 cm^{-1} appear to be more pronounced in the spectra measured at low temperatures. An interesting variation of the spectra occurs in the case of the peaks close to 300 cm^{-1}, where the two peaks that were previously strongly overlapped become more easily distinguished, and another peak at 297 cm^{-1} can be resolved. Another peculiar observation from the low temperature measurements lies in the presence of a peak at 338 cm^{-1}, which cannot be observed in spectra measured at room temperature under any excitation wavelength due to strong overlapping with the intense peaks at 300 and 310 cm^{-1}. This peak is preliminary assigned to the B_{2g} active mode in accordance with the first principle calculations.

Finally, it is worth mentioning the peaks at 171 and 187 cm^{-1}, which were resolved only in the spectrum measured at 20 K, and in the spectra measured at room temperature only a broad band could be measured at 175 cm^{-1}. The latter peak was also observed in previous publications but was directly assigned to the one-phonon mode of the Sb_2S_3. However, both the first-principles calculations presented in the current study and by Liu et al.[17] show a gap free of phonon states in the range of 160–180 cm^{-1}. This, together with a reduction of the relative intensity of these peaks in the spectrum measured at 20 K, allows suggesting the multi-phonon (MP) nature of these two peaks, which can be a combination of several one-phonon peaks from the low wavenumbers range.

Analysis of the Sb_2S_3 thin films

The Raman scattering spectra of two analyzed thin films exhibit typical spectra of Sb_2S_3 compound, with insignificant variations between the films (Figure S8). It should be noted that for each sample the spectra were measured in at least 12 points, and no significant variations of the spectra were found. The XRD difractograms were measured in the complete devices, for which the initial Glass/FTO/Sb_2S_3 structures were completed with buffer (CdS) and windows (i-ZnO/ITO) layers. In the resulted difractograms of the full devices based on the two discussed thin films (see Figure S10), apart from a clearly defined reflection of FTO and ITO phases, corresponding to back and front contact of the solar cells, two phases can be seen in the Sb_2S_3 layer. The first one is the Sb_2S_3 phase, for which the Rietveld refinement yielded a clear improvement of crystallite size with increase of annealing temperature (from ~50 nm for 300°C up to ~150 nm for 375°C). However, no change in the preferential crystalline orientation was observed, which was mainly along [301] and [201] directions, in agreement with the results obtained from Raman spectra analysis. Additionally, the pure Sb phase was observed in both samples (~22% for 300°C, and ~3% for 375°C), which was found to be concentrated on the back side of the layer due to the non-optimal sulfurization conditions. The later, however, has no influence on the Raman spectra analysis, due to surface nature of this technique.